Tribol Lett
DOI 10.1007/s11249-008-9319-0

ORIGINAL PAPER

Dynamics in the Bridged State of a Magnetic Recording Slider

Thomas E. Karis · Xing-Cai Guo · Jia-Yang Juang

Received: 24 July 2006 / Accepted: 12 March 2008

Abstract A novel region of tribological interaction is explored by inducing near contact between the magnetic recording slider and disk. In this study, we performed frictional measurements over a wide range of subambient air pressure and disk rotation rate. Since the slider is supported over the disk by an air bearing, it has been found that cycling from ambient to subambient and then back up to ambient pressure over several minutes of time forms a frictional hysteresis loop. The high-friction branch of the loop, referred to as the bridged state, is characterized by an average frictional displacement and resonant vibration of the suspension mount assembly. The bridged state is currently employed for accelerated wear testing of magnetic slider/disk/lubricant systems. Future magnetic recording systems designed to operate at increasingly lower physical spacing will need to take into account these frictional forces which accompany the incipient contact between the lubricated disk and slider with finite surface roughness. A single degree of freedom model is solved to determine the equivalent dynamic friction force on the slider as an impulse series with random impulse frequency and amplitude from the measured frictional displacement in the bridged state. The mean slider-disk spacing in the bridged state is derived from the experimental friction force, the spacing probability density function, and the adhesion stress from the Lifshitz model for dispersion interaction energy.

T. E. Karis (✉) · X.-C. Guo · J.-Y. Juang
San Jose Research Center, Hitachi Global Storage Technologies,
3403 Yerba Buena Road, San Jose, CA 95135, USA
e-mails: Tom@tekdat.com; Tom.Karis@hitachigst.com

X.-C. Guo
e-mail: Xing-Cai.Guo@hitachigst.com

J.-Y. Juang
e-mail: Jia-Yang.Juang@hitachigst.com

Keywords Applied tribology · Magnetic data storage · Component and machine tribology · Magnetic data disks · Friction and energy conservation · Friction mechanisms

1 Introduction

Advances in storage technology rely upon a stable and reproducible low friction on the slider to allow precise servo mechanical positioning of the read and write elements on the data tracks, to maintain uniform magnetic read back signal amplitude, and to avoid mechanical damage of the disk and slider surface layers. Intermittent contacts between the slider and the disk increase the chances of forming scratches or magnetic erasure by impact with the disk [1, 2].

On the other hand, many researchers are investigating air-bearing sliders that incorporate some contact into their design. Understanding the origins of the contact force between the slider and the disk is currently at the frontiers of this work. Contact forces have been treated according to several different approaches. Intermolecular forces were incorporated into an air-bearing model to account for experimentally observed flying height hysteresis [3, 4]. The majority of publications postulate a liquid lubricant meniscus as the primary contribution to the friction force between the low flying or contacting slider and the disk [5–11].

Interaction force between the low-flying slider and disk may also arise from liquid bridges, which are expected to form between two lubricated surfaces in close proximity [12, 13]. From molecular dynamic simulations, shearing of molecularly thin layers of lubricant alone is expected to produce frictional force oscillations on the picoseconds time scale [14, 15]. The bridged state is observed experimentally by decreasing the disk rotation rate to decrease the air-bearing lift force causing the slider to approach the disk surface from above [16–18]. The bridged state can also observed by lowering the air pressure in a disk drive [19] or tester [20, 21]. It is now understood that when the slider approaches the disk from above, the first contacts are between capillary waves on the lubricant surface [22]. Consequently, the disk lubricant molecular weight, end groups, bonding, and disk surface roughness determine the mean spacing at which the bridged state is observed [23]. The bridged state is characterized by a high friction and vibration of the slider, suspension, and mounting assembly.

The touch down pressure (TDP) is the pressure at which the slider-disk interface enters the bridged state and friction and vibration of the slider suddenly increases with decreasing pressure; the take off pressure (TOP) is the pressure at which the slider resumes normal flying with increasing pressure. Most studies of the (sub ambient) hysteresis loop in magnetic recording are focused on determining the dependence of the TDP and TOP on parameters such as lubricant molecular weight, end groups, bonding, ambient humidity, disk roughness, and slider geometry. These investigations provide phenomenological results leading to semi-empirical hypothesis regarding the nature of the bridged state, and the quality of the magnetic recording slider-disk interface.

This study explores the physics of the bridged state at the TDP. Information about the nature of the forces on the slider in the bridged state is derived from the frictional displacement and a single degree of freedom model for the load beam and slider suspension assembly.

The meniscus concept has recently been applied to the tribology of lubricated magnetic recording head and disk interfaces, e.g., [24, 25]. We find that: (a) The meniscus volume is less than the volume of one Ztetraol 2000 lubricant chain; (b) The wetted perimeter is the length of about 8 lubricant chains stretched end to end; and (c) The wetted length is about 24 lubricant chain lengths. Hence the formation of a meniscus involves the rearrangement of about two dozen chains, and the volume of the curved mensicus surface is less than one lubricant molecule. At the mid-range velocity of 10 m/s, then time between asperity contacts is 38 ns, and the duration of an asperity contact is 8.4 ns. For the lubricant to flow out from between the two asperities down to one flat molecular layer equal to the atomic diameter of the chain and into the meniscus, the initial average lubricant flow velocity estimated using the cross-sectional area defined by the contact length and the disk lubricant film thickness is 5.4 m/s. The shear rate, for a 1-nm-initial film thickness is then 5.4×10^{9} 1/s. Hence the meniscus model is subject to the same constraint of viscoelasticity as a shear flow for molecularly thin and highly bonded liquid films. It is not physically meaningful to invoke shear flow within asperity contacts lubricated by molecularly thin and highly bonded lubricant films because our process time scale of $1/\dot{\gamma} = 1.8 \times 10^{-10}$ sec for the shear is much less than the 10^{-5} s characteristic viscoelastic relaxation time for PFPE lubricant chains [26]. We show that a molecular adhesion model derived from dispersion force interaction through the Liftshitz theory is more appropriate at the time and length scales of asperity interactions in the bridged state.

Recent investigations have found that there is a critical flying height below which the onset of lubricant accumulation on the slider and depletion from the disk surface is observed [27]. The existence of a critical flying height is accounted for by intermolecular forces and transport of lubricant molecules across the air-bearing gap. In our molecular adhesion model which incorporates surface roughness we show that lubricant transfer is expected to vary almost exponentially with mean spacing between the lubricated disk and slider surfaces.

2 Experimental

2.1 Materials and Apparatus

The disks were typical 95-mm-diameter magnetic recording diks made on AlMg substrates with a carbon overcoat and 0.8 nm of Ztetraol 2000 lubricant. The chemisorbed fraction of lubricant was 80% measured by rinsing with Vertrel XF and measurement with reflection Fourier Transform Infrared Spectroscopy. Finished disk rms roughness was 0.33 nm from atomic force microscopy. Sliders were typical pico sliders made of N58 (Al_2O_3/TiC) ceramic material and overcoated with 2.5 nm of carbon. The slider body was 1.2 mm long, 1 mm wide and 0.3 mm thick. The pivot point was centered on top of the slider body. The normal load applied by the 4–micron-thick steel suspension on the slider was 2.5 grams (or 24.5 mN). The suspension was mounted on a load beam as shown in Fig. 1a. A strain gage was epoxy bonded to the metal load beam, and the suspension was bolted onto the lower end of the load beam with the back of the slider 11 mm from the suspension mounting point on the load beam. Force f applied to the assembly by the head disk interface of the slider gives rise to load beam deflection x.

Frictional hysteresis loop measurements were performed inside a sealed disk tester with a controlled leak (CETR Olympus). For these tests, the radial position was 30.6 mm (near the middle diameter of the disk), and the skew angle was close to zero degrees. The disk rotation was started at 7,200 rpm with the slider suspension on the load/unload ramp just off the edge of the disk. The slider was accessed to the test radius; the rotation rate was adjusted lower as specified between 800 and 7,200 rpm. The air pressure was controlled with an analog vacuum pressure controller

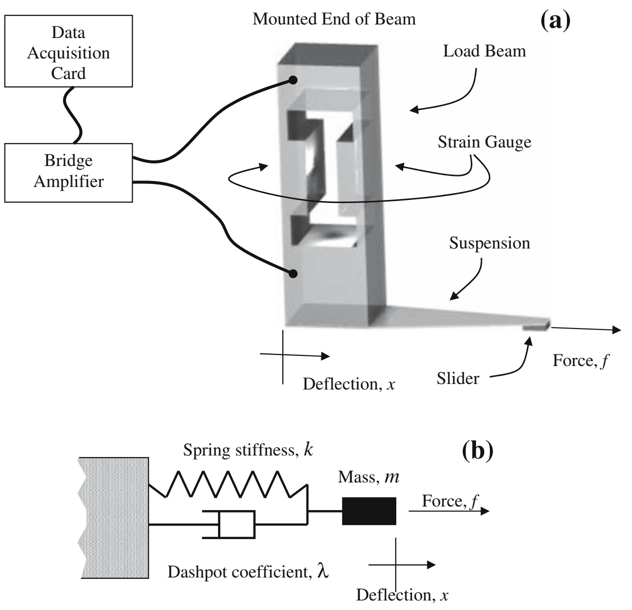

Fig. 1 (**a**) Schematic diagram of the load beam and slider suspension assembly drawn to scale, and (**b**) equivalent damped single degree of freedom linear spring mass system

(MKS Instruments type 640 with a type 167 power supply/readout). Pressure setting and measurement of the frictional displacement was performed with National Instruments LabView software on a PC with interface cards. The pressure inside the tester was varied stepwise linearly from ambient (100 kPa) toward 15 kPa and back up to ambient over about 3 min time in approximately 1 kPa increments. After each pressure decrement/increment, the average frictional displacement of the strain gage and peak vibration amplitude were recorded (4,000 samples at 20 kHz).

At the end of the test, the rotation rate was increased to 7,200 rpm and the slider was accessed back to the load/unload ramp before stopping the disk rotation.

During some of the tests the pressure was manually controlled to enter the bridged state and then capture 200 ms friction versus time apertures for subsequent analysis. All the tests were done with the same slider and at the same radial position on the disk.

Following the subambient pressure tests the disk surface was examined for wear particles, lubricant removal and redistribution, and surface topography with a KLA Tencor Candela 6100 Optical Surface Analyzer (OSA). For survey scans, the encoder multiplier was 32× and the step size was 3 microns, for a pixel size (resolution) of 3 microns radially and 6 microns circumferentially. Lubricant thickness was studied with the Q phase image (QPh, which is similar to an ellipsometric measurement). A calibration was performed to determine the percentage variation in QPh with lubricant thickness.

The Q scattered image (QSc) was examined to look for wear debris (similar to dark-field microscopy). The QSc images can detect particles as small as 100 nm in diameter, although the scattering volume is much larger than the actual particle size due to pixel blooming in the CCD camera and the discrete pixel area.

The QZc image was employed to measure surface topography in the test tracks. Images with 3 microns circumferentially and 1 micron radially were integrated in the circumferential direction to obtain surface profiles. The surface level was calibrated with disk surface topography measured with a Tencor stylus profilometer (Model P-12 Disk Profiler, with tip radius of 2 microns).

Slider surface topography before and after the tests was measured with a Veeco Wyco optical profiler.

2.2 Friction Force Measurement

2.2.1 Dynamic Model

A dynamic model for the load beam and slider suspension assembly was developed to provide insight into the nature of the frictional forces acting on the slider which produce the observed voltages measured from the strain gage mounted on the load beam. The load beam spring constant, resonant frequencies, and damped oscillations were calculated with ANSYS general purpose finite element analysis software (ANSYS, Inc. http://www.ansys.com). For the ANSYS calculation the damping coefficient was 0.5%;

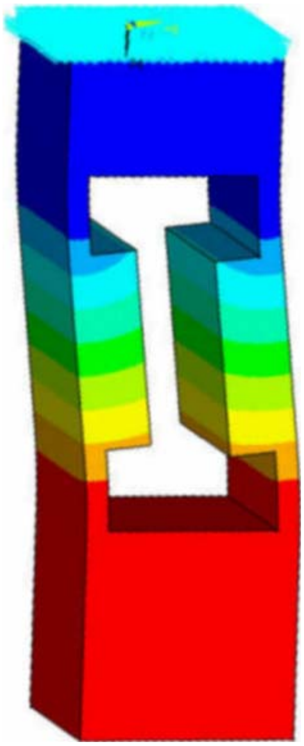

Fig. 2 Finite element model showing the primary deformation of the load beam during frictional displacement

Table 1 Dynamic mechanical properties of the load beam and head suspension assembly

Definition	Symbol	Value		
		Calculated	Measured	Units
Lumped parameter	b_0	4.04E + 8	3.71E + 8	1/s^2
Lumped parameter	b_1	201	200	1/s
Damped oscillation frequency	$\beta/2\pi$	3,200	3,067	1/s
Spring constant	k	1.32E + 5	–	N/m
Effective mass	m	3.27E-4	3.55E-04	kg
Effective dashpot coefficient	λ	0.066	–	N-s/m

Calculated values are from the finite element solution for the load beam alone. Measured values are from a fit of the single degree of freedom model to the damped oscillations of the load beam and slider suspension assembly

tensile modulus was 70 GPa; and density 2,700 kg/m^3. The fundamental deformation mode of the load beam is parallel to the disk surface, as shown in Fig. 2. The parallel shear mode determined by the design of the load beam shape prevents small displacements from changing the elevation of the suspension during friction measurement. The calculated spring constant and resonant frequency for the load beam are given in Table 1. For comparison with the experimental measurement system, the damped oscillations of the load beam from an initial displacement are shown in Fig. 3a.

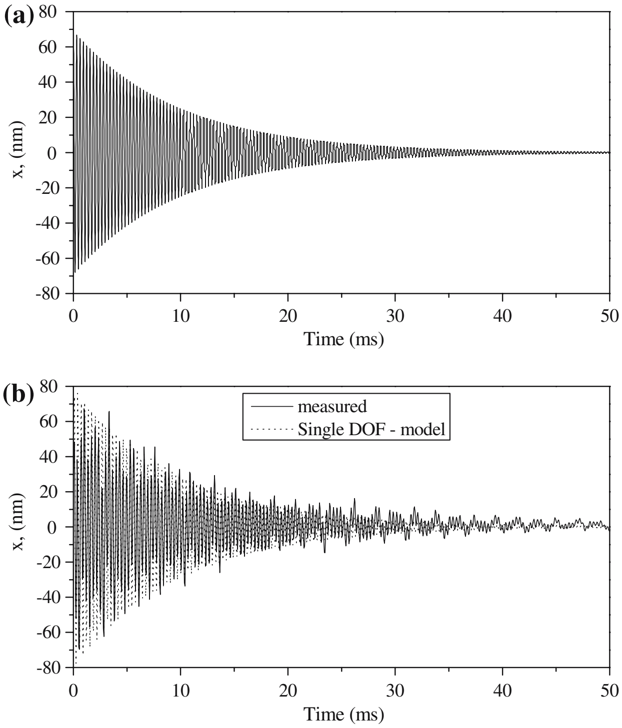

Fig. 3 Damped oscillations of the load beam (**a**) calculated from solid body mechanics with ANSYS and (**b**) following a tap on the arm mount of the load beam and head suspension assembly with the superimposed fit of the single DOF model

A dynamic model was adopted to provide insight into the relationship between the measured load beam deflection and the force at the slider-disk interface. The single degree of freedom linear spring mass dashpot equivalent mechanical system is shown schematically in Fig. 1b. The dynamic response of this system is described by Eq. (1):

$$\frac{d^2x}{dt^2} + b_1\frac{dx}{dt} + b_0 x = \hat{f}(t) \tag{1}$$

where $b_1 = \lambda/m$, $b_0 = k/m$, and the excitation $\hat{f}(t) = f(t)/m$; m is the effective mass, x is the strain gage deflection, t is time, λ is the dashpot coefficient, k is the spring stiffness, and $f(t)$ is the excitation force. The system is further characterized by the damping coefficient $\zeta = \lambda/(2\sqrt{km})$. Coefficients b_1 and b_0 were determined by fitting the response to a single excitation force impulse $\hat{f}(t) = \hat{f}_1\delta(t)$,

$$x(t) = \left(\hat{f}_1 \big/ b_0\right) e^{-\alpha t} \sin(\beta t), \tag{2}$$

where $b_1 = 2\alpha$, $b_0 = \beta^2 + \alpha^2$, $\hat{f}_1$ is the impulse amplitude, and $\delta(t)$ is the unit impulse or Dirac delta.

2.2.2 *Calibration*

For low frequency or static force measurements the strain gage bridge amplifier voltage is usually calibrated directly in grams or Newtons by applying various known weights or pull forces to the suspension. For this purpose, a thread was run over a ball bearing pulley with hooks on each end made from small pieces of wire. One end was attached to the suspension with the pull force aligned along the axis of deflection. Weights were hung on the other end of the thread in 1 gram increments from 0 to 8 grams. The mass calibration linear slope was 0.5 volts/gram with $R^2 = 0.9998$.

Coefficients b_1 and b_0 were determined by lightly tapping the pivot arm housing the load beam and slider suspension assembly with the slider elevated away from the disk and load/unload ramp. The measured impulse response of the assembly is shown in Fig. 3b. The dashed curve shows the fit of the single DOF model parameters b_1 and b_0 in Eq. (1) to the damped oscillations with Eq. (2). The experimental single DOF model parameters and coefficients are listed in Table 1. The effective mass m was calculated from b_0 and the k value from the ANSYS calculation in Table 1. The effective mass is also a fitting parameter, and does not reflect the actual mass of the system.

The amplitude spectra calculated from the Fast Fourier Transform (FFT) of the damped oscillations in Fig. 3 are shown in Fig. 4. The fundamental resonance peak frequency calculated for the load beam with ANSYS is slightly higher than the measured peak frequency. This difference is due to

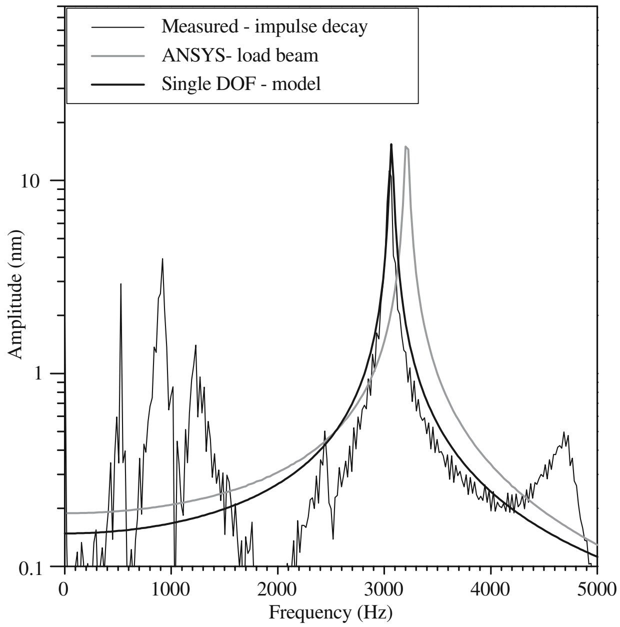

Fig. 4 Amplitude spectrum of the measured impulse response to a tap on the arm mount of the load beam and head suspension assembly, ANSYS solution for the load beam, and the fit of the single DOF model to the measured impulse response

the contribution of the strain gages mounted on the load beam, which were not included in the solution. Several other resonances are apparent in the measured impulse response in Fig. 4. The lower frequency resonances are from the pivot arm housing the load beam. The higher frequency resonance is bending of the slider suspension assembly. In the region of the fundamental resonance, the single DOF model accurately fits the measured peak, and has a similar shape to the ANSYS solution. As will be shown later, the fundamental resonance peak dominates the amplitude spectrum measured in the bridged state.

3 Results

3.1 Frictional Hysteresis Loop

The typical pressure, average friction, and frictional vibration as a function of time during the measurement are shown in Fig. 5a. The hysteresis loop shown in Fig. 5b is obtained by replotting the friction and vibration as a function of pressure during the test. Arrows indicate the progression along the loop with time. As the pressure is being decreased while the slider is flying, the frictional displacement and vibration are both very low. At the TDP, the average frictional displacement and vibration increase discontinuously from one pressure decrement to the next. As the pressure is being increased above the TDP along the increasing pressure branch of the hysteresis loop, the average frictional displacement and vibration remains high up to the TOP, or until the test ends near atmospheric pressure at 90 kPa.

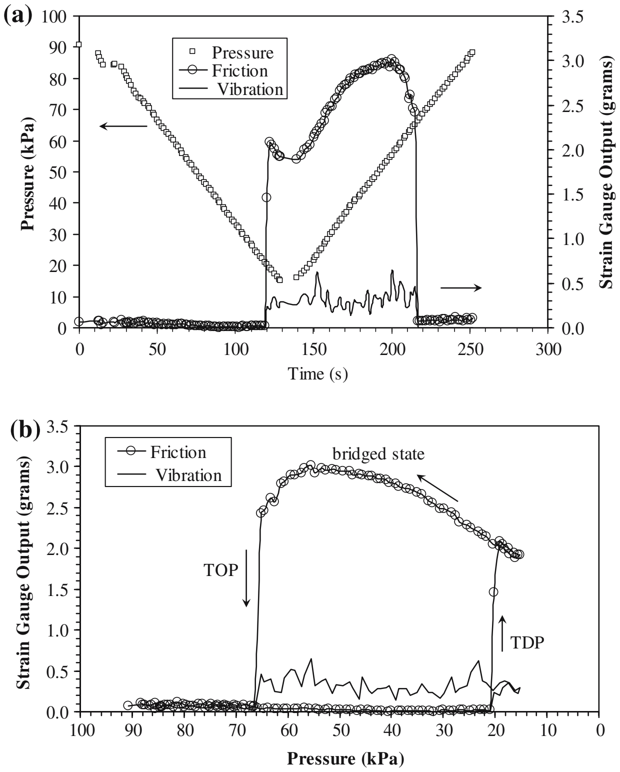

Fig. 5 Pressure, average friction force, and friction force vibration amplitude versus time (**a**) and versus pressure (**b**) during a typical hysteresis loop measurement. Rotation rate 7,200 rpm

The frictional hysteresis loop measured at several different disk rotation rates (linear velocities) is shown in Fig. 6. The direction of traversal along each hysteresis loop is indicated by the arrows. At the lowest two rotation rates, 1,800 and 1,300 rpm, the bridged state persisted up to the end of the test cycle, and the bridged state average frictional displacement was significantly higher at 1,300 rpm.

Both the TDP and TOP increased with decreasing disk rotation rate. The TOP and TDP are shown plotted as a function of the disk linear velocity in Fig. 7. The two points at the highest linear velocity are from two separate runs, showing the good reproducibility of these measurements. The arrows over the open box symbols in Fig. 7 indicate that no TOP was observed up to 90 kPa at these two velocities. The hatched region in between the TDP and TOP curves in Fig. 7 is the bi-stable region in which the slider is flying during the decreasing pressure branch of the hysteresis loop and in the bridged state during the increasing pressure branch of the loop measurement. The dashed line in Fig. 7 shows a fit of the Reynolds equation with first order gas rarefaction [28] to the TDP = P_c, as a function of velocity, V with $P_c = ah_c/\left(V - bh_c^2\right)$, where a

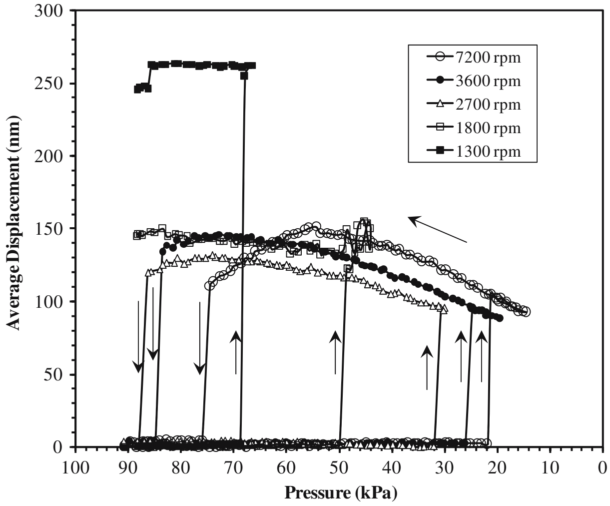

Fig. 6 Average displacement during hysteresis loop measurement at several different disk rotation rates. There was no TOP at the lowest two rotation rates

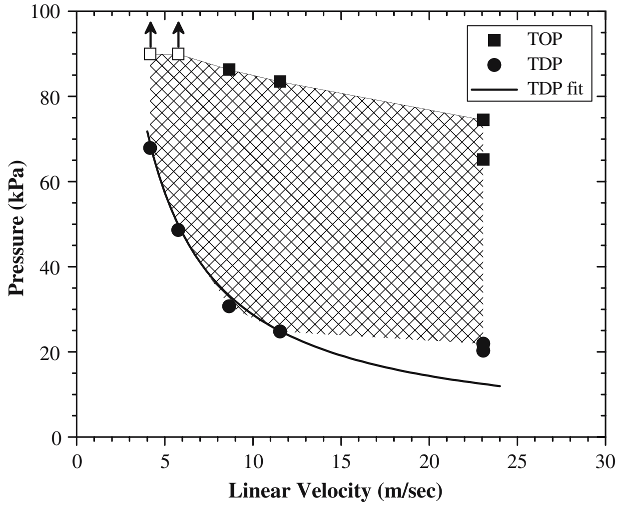

Fig. 7 TDP and TOP as a function of linear velocity from Fig. 6. The vertical arrows indicate that there was no release from the bridged state at the two lowest rotation rates. The smooth curve shows a fit of the TDP data to Reynolds equation with first order gas rarefaction. The crosshatched region is bi-stable, flying along the decreasing pressure branch, bridged along the increasing pressure branch

and b are lumped parameter coefficients that were determined by regression fit to the data, and h_c is the flying height at P_c. At the highest velocity, or at the lowest TDP, the fit deviates below the data due to the increasing importance of higher order rarefaction effects. The higher order contribution of the flying height, b, was made negligibly small by the regression. This shows that h_c is independent of linear velocity and pressure. We show later that h_c is the difference between the mean solid surface separation in the bridged state and the total lubricant thickness (on the disk and slider).

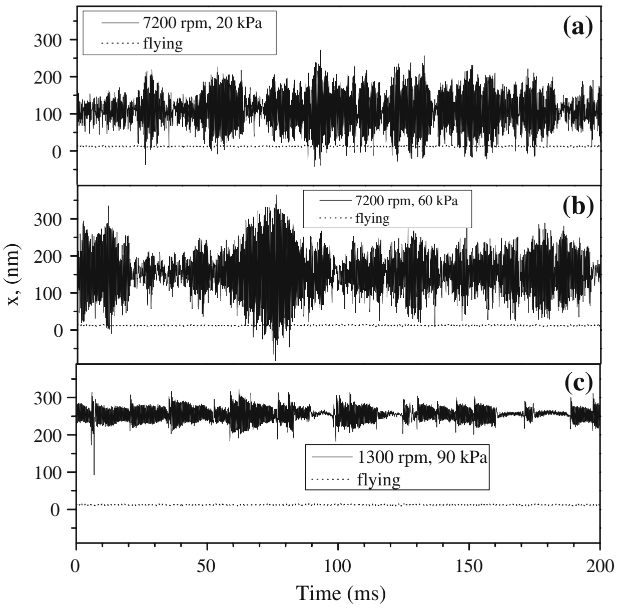

Fig. 8 Displacement versus time over 200 ms time intervals (**a**) 7,200 rpm, 20 kPa, (**b**) 7,200 rpm, 60 kPa, and (**c**) 1,300 rpm, 90 kPa. The lower curve in each chart shows the baseline displacement measured while flying state at 7,200 rpm and 70 kPa

3.2 Displacement Signal in the Bridged State

Typical displacement versus time apertures recorded at different rotation rates and pressures are shown in Fig. 8. The upper trace which is in each figure shows displacement when the slider is in the bridged state. The displacement in the bridged state is characterized by an average displacement and vibration. Viewed in real time with an oscilloscope synchronized to the spindle rotation, the displacement signal in the bridged state appeared as a clear tone with irregular amplitude modulation. The average displacement and vibration increased with increasing pressure from 20 to 60 kPa at 7,200 rpm, Fig. 8a, b. The bridged state at 1,300 rpm and 90 kPa (nearly atmospheric pressure!) had a higher displacement with lower vibration, Fig. 8c. The lower dotted curves in Fig. 8 show the baseline displacement with the slider flying at 7,200 rpm and 70 kPa. In the flying state, the average baseline displacement is 12 nm.

3.2.1 Autocorrelation

The autocorrelation of the displacement signal was calculated for the fluctuating component of the displacement in the bridged state. The autocorrelation of a signal $x(t)$ is defined by

$$R_{xx}(\tau) = \int_{-\infty}^{\infty} x(t)\,x(t+\tau)\,dt, \tag{3}$$

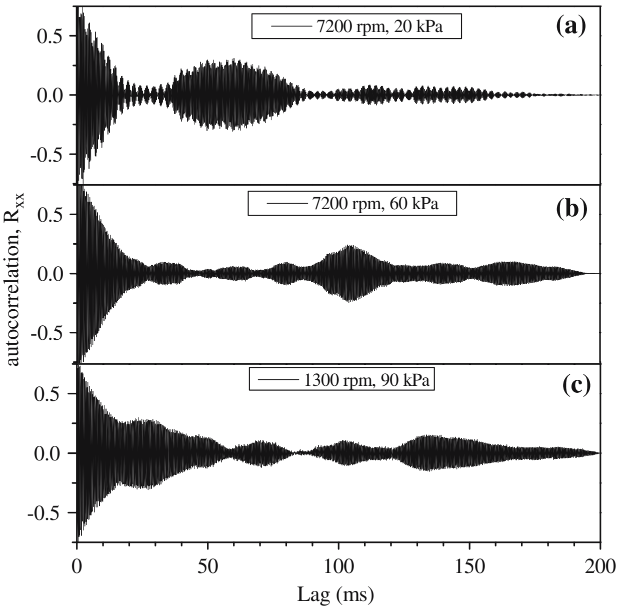

Fig. 9 Autocorrelation of the fluctuating displacement in Fig. 8

where τ is the lag (time). Repetitive patterns in a signal $x(t)$ show up as coherence structure in the autocorrelation function $R(\tau)$ *vs.* τ.

The autocorrelation plots of the fluctuating displacement from Fig. 8 are shown in Fig. 9. In this case, the model simulation later shows that apparent coherence times arise randomly from patterns of constructive and destructive interference among the driven oscillations of the assembly. There is no coherence peak time at multiples of the disk rotational period.

3.2.2 *Amplitude Spectra*

The amplitude spectra of the fluctuating displacement signals in Fig. 8 are shown in Fig. 10. The smooth curves in Fig. 10 show the fit of the single DOF model impulse response to the fundamental resonance peak of the measured displacement. The gray trace shows the fit of the single DOF model driven with random impulses as will be explained in the Discussion. Frequency components at multiples of the disk rotational frequency were not observed in any of the spectra. Thus the resonant vibrations did not appear to be driven by a particular location on the disk surface.

3.3 Optical Surface Analysis of the Tested Track

All of the above tests were performed on the same test track. The first subambient pressure hysteresis loop test was repeated at the end of the test series to verify reproducibility. If any overcoat wear debris is generated in the test track, there is no TDP and the steady displacement and vibration characteristic of the bridged state is not observed even down to the lowest pressures. A minute quantity of atmospheric particle contamination dramatically reduces or eliminates the hysteresis loop and friction at low pressure [21].

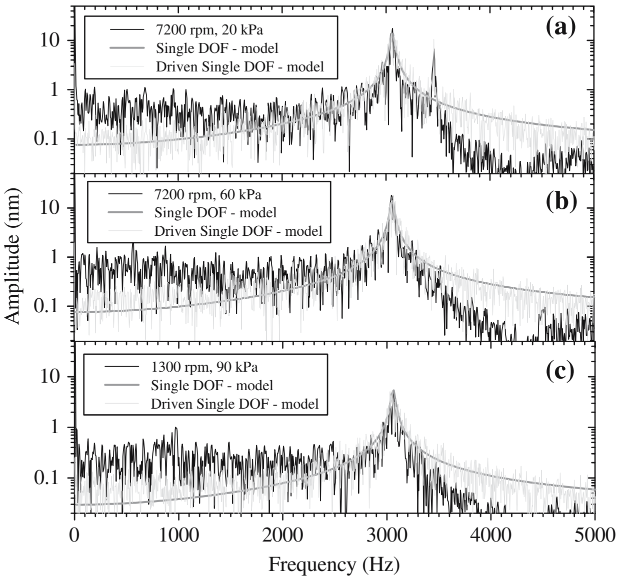

Fig. 10 Amplitude spectra of the fluctuating displacement versus time showing the effect of disk rotation rate (linear velocity) and pressure from the data in Fig. 8. The thick gray trace shows the fit of the single DOF model impulse response, and the thin gray trace shows the fit of the dynamically driven single DOF model to the measured spectrum

Sensitive analysis was performed on the test track in order to further verify the absence of particulate wear debris and to measure any lubricant removal or redistribution. Scattering images with the circumferential laser (QSc) verified the absence of wear debris particles on the disk. With the radial laser, QSc images detected the usual substrate texture groove pattern (formed in the substrate to improve the signal to noise ratio of longitudinal magnetic recording media [29]), but no scratches were found in the carbon overcoat. Visual inspection of these QSc images of the test track revealed no evidence of abrasion from slider-disk contact during the subambient pressure tests.

3.3.1 *Lubricant Profile*

The test track was visible in the QPh image. As mentioned, this image is comparable to an ellipsometric measurement. At each radius, QPh was averaged over 8.2 mm circumferentially along the track. The apparent variation in the lubricant film thickness as a function of radial position across the test track was calculated from the QPh image data using a previously determined calibration factor, and is shown in Fig. 11. There are two regions of apparent lubricant depletion, which coincide with the location of the

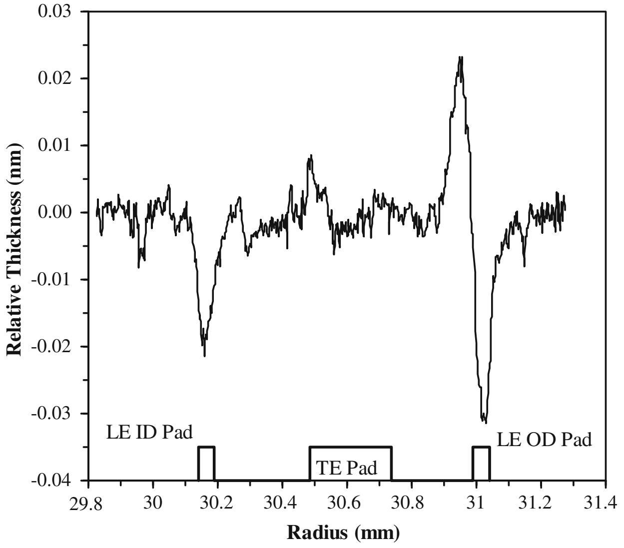

Fig. 11 Relative (lubricant) thickness profile across the test track at the end of the tests from the optical surface analyzer (upper trace). Location of the air-bearing pads shown on the same horizontal scale, vertical not to scale (lower trace). The location of the pads on the slider air-bearing surface are shown in Fig. 12

air-bearing surfaces. There are also two peaks of apparent lubricant buildup. Since these measurements were performed several weeks after the last subambient pressure test on this track, lubricant reflow by surface diffusion would be expected to level the film thickness. An apparent film thickness increase could be accounted for by the formation of degraded lubricant end groups [30]. The apparent film thickness variation could be due to lubricant chain length reduction by degradation, a reduction in the carbon overcoat thickness, or changes in the index of refraction of any surface layers.

However, even though the apparent lubricant film thickness variations can be measured by the extremely sensitive optical surface analyzer, these changes are much less than the lubricant chain molecular diameter, which is 0.4–0.6 nm (depending on its conformation on the surface). Comparable effects are produced by variations in submonolayer water adsorption [31]. Lubricant removal and redistribution amounted to less than 6% of the total lubricant film thickness, and it is less than the atomic diameter of the fluorine atom constituent of the PFPE lubricant chain.

3.3.2 Test Track Indentations

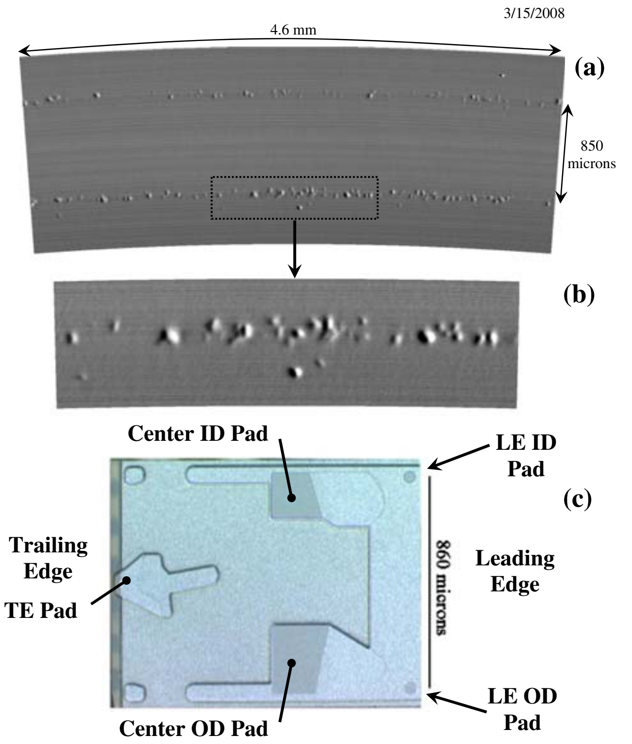

Fig. 12 Optical surface analyzer QZc image of the test track showing indentations made by slider impacts with the disk surface. (**a**) Section of polar view, (**b**) zoom in to a region of the ID track, polar view, and (**c**) optical micrograph of the slider ABS showing the leading edge and center ID and OD pads and the trailing edge pad. CCW disk rotation is from right to left

Even though there was only very little lubricant redistribution and no evidence of wear debris particles or abrasive wear in the scattering images, surface topography defects within the test track were evident in the QZc image. A section of the polar view of the QZc image including the test track is shown in Fig. 12a, and a zoom image is shown in Fig. 12b. Circumferential lines in the image are probably from pad burnishing [32] that is performed on all disks after lubrication to remove asperities that protrude above a specified glide height. The spacing between the tracks of defects coincide with the spacing between the center of the valleys in the lubricant thickness profiles in Fig. 11, and the spacing between the LE pads on the slider as shown in Fig. 12c. Since the polar view renders the image without distortion, Fig. 12b shows that the individual defects are nearly circular.

An algorithm was developed to count the number of defect sites by recognizing that a site always exhibits a characteristic dark (negative) followed by a light (positive) variation in the QZc image. The inner track contained 2,500 while the outer track contained 1,968 defects.

Typical surface profiles measured through the center of a typical defect site by the OSA (integrated QZc) and profilometer are shown in Fig. 13a. The defect sites were shallow indentations 50–100 microns across and 5–15 nm deep.

If the disk and slider were moving with respect to one another during the formation of the defect, they would appear as a scratch, or at least be significantly elongated in

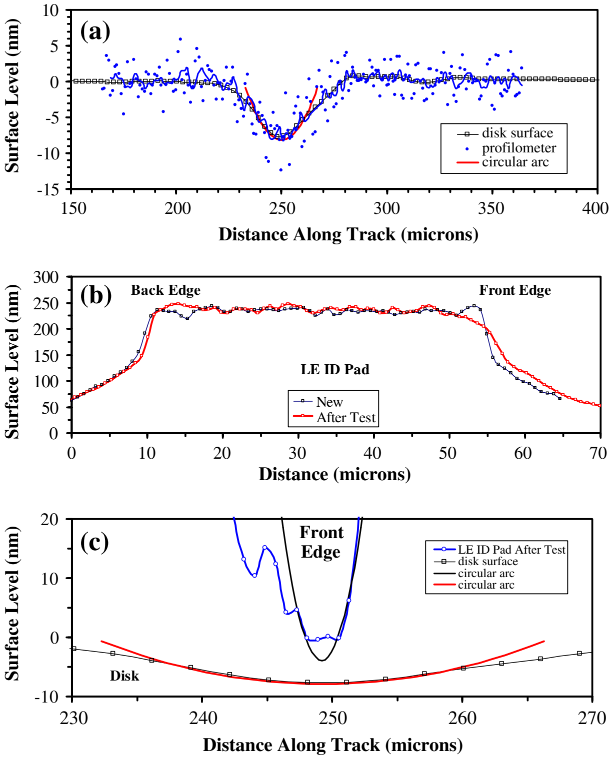

Fig. 13 (**a**) Surface topography profiles measured across the center of a test track indentation. Integrated QZc is shown by the open squares, small filled circles are the profilometer trace, and the heavy smooth cusp is the circular arc profile, circumferential direction, (**b**) Surface profile from back to front across the leading edge pads on a new slider and the slider after subambient pressure friction test, and (**c**) tested slider leading edge ID pad front edge corner from (**a**) tilted up and scaled for comparison with indentation (**a**). Slider tilt angle of approach to the disk is −7 mrad about the pivot point

the sliding direction. The curvature radius of the indentations was determined by fitting a circular arc to the central portion of each profile. The curvature radii, listed in Table 2, vary from 15 to 30 mm. Since the aspect ratio of the curvature radii (circumferential/radial) was between 1 and 2, there was not much relative motion between the slider and disk during the indentation process. This small amount of asymmetry could be due to asymmetry in the shape of the contact point on the slider (see below).

In the following, the depth and radius of an indentation is employed to calculate the load and tip radius of a spherical indenter that would be required to form that indentation according to $P_{\max} = H \times A_r$, where $P_{\max}$ is the maximum load, A_r is the residual area, and H is the nano indentation hardness. For shallow indentations with the depth $d << $ radius r, such as those found on the test tracks, the residual area $A_r \approx 2\pi rd$. The residual areas for the indentations are listed in Table 2. The nano indentation hardness measured on NiP plated AlMg substrates is typically 8+/−0.5 GPa. The hardness and residual area were used to calculate the indentation load, which is given in the last two columns of Table 2. The load is surprisingly high considering the much smaller mass of the slider. Indentations of the same size and shape were formed by exposing the same disks to ultrasonic cavitation bubbles in the ultrasonic cleaning station of a disk washer.

3.3.3 Slider Pad Wear

The presence of indentations on the disk test track aligned beneath between the leading edge pads of the slider implies that the leading edge pads front edge occasionally made contact with the disk surface. The surface profile of the pad edge was measured with a Wyco optical profilometer. A line profile of the surface height from back to front of the LE ID and OD pads on the new and tested slider is shown in Fig. 13b. The Wyco images detected rounding, with 14–22 nm removed from the LE pad front corner.

In order to see if the indentation matches the LE pad front corner, the two profiles are shown together in Fig. 13c. The closest match between the curvature of the pad and that of the indentation was for an incident pitch angle of −7 mrad with rotation about the center of the slider (pivot point). The LE pad front corner appears distorted in Fig. 13c because of the rotation and the difference between the scales of the horizontal and vertical axes. A circular arc fit to the pad corner profile (smooth upper curve in Fig. 13c) had a curvature radius of 0.2 mm. The LE pad front corner curvature radius is two orders of magnitude less than that of the disk indentation. We estimate that the two surfaces could have been in contact with negligible relative motion for only about 1 micron. Given that the relative velocity was between 4 and 23 m/s, the time allowed to form the indentation is around 40 ns.

Table 2 Characteristic length scales of the indentations measured in the test tracks

Site	Curvature radius		Aspect	Depth	Residual area	Indentation load	
	Circumferential (mm)	Radial (mm)	ratio	(nm)	(m^2)	(N)	(grams)
1	30	22	1.36	8.4	13.6E-10	10.9	1,114
2	20	15	1.33	8.1	8.9E-10	7.1	727
3	30	15	2.00	7.9	11.1E-10	8.9	908
4	30	30	1.00	6.6	12.4E-10	10.0	1,016

The indentations do not affect the frictional hysteresis loop because they are not aligned with the trailing edge pad. The indentations were not associated with particle generation or material removal from the disk. One very interesting observation is that the radius of the indentations formed in the test track on the disk surface under the LE pads was significantly larger than the radius of the contact point at the leading edge of the pad. The origin of the indentations is revisited near the end of the Discussion.

4 Discussion

4.1 Dynamic Friction Force

Due to the high mass and low stiffness of the assembly, higher frequency components of the excitation cannot be faithfully recovered from the measured displacement signal. In order to provide some insight into the dynamic properties of the excitation, an effective excitation was employed. If the effective excitation reproduces the appearance of the measured displacement, fits the amplitude spectrum and is consistent with the experimental autocorrelation function, we can say that the actual excitation is equivalent to the effective excitation from the viewpoint of the assembly. The model displacement was calculated in response to a series of force impulses with randomly modulated period and amplitude $\hat{f}(t) = \hat{f}_0 + \sum_{n=1}^{N} \hat{f}_n \delta(t - nT_n)$. The solution is written as

$$x(t) = (1/b_0)\hat{f}_0 + (1/b_0)\sum_{n-1}^{N} \hat{f}_n U(t - nT_n) e^{-\alpha(t - nT_n)} \sin\left[\beta(t - nT_n)\right], \quad (4)$$

where the first term is the average displacement due to the steady force component, the second term is the fluctuating component, and $U(t)$ is the Heaviside step function.

Values of $x(t)$ were calculated from Eq. (4) at the experimental data acquisition rate (4,000 samples at 20 kHz), and the solution was allowed 50 ms time to reach steady state (relaxation time $1/\alpha = 10$ ms). The model excitation properties were varied to determine the range of values, which reasonably approximated the experimentally observed displacement properties in the bridged state. The bursts in the excitation amplitude, Fig. 8, and the structure of the autocorrelation, Fig. 9, were reproduced when: $\hat{f}_n$ was uniformly random between 0 and $\hat{f}_m$; and the time between force impulses T_n was uniformly random in the interval $T(1 \pm r_n)$ with $0 \leq r_n \leq 1$. Even harmonics were removed from the amplitude spectrum when $r_n \geq 0.2\%$.

The simulation parameters which closely approximated the experimental bridged state displacement, FFT amplitude spectrum, and autocorrelation are listed in Table 3. From the model simulation results: The steady force component was larger than the fluctuating component, even though the displacement fluctuations are comparable to the mean displacement at the lower pressures. As the rotation rate (velocity) decreased, and the pressure increased, the period between force excitations increased, and they were more randomly distributed over time. The displacement fluctuations are large because the envelope of the modulation term in Eq. (4) is approximately $\left(\hat{f}_n/b_0\right)/(2\alpha T)$. Physically this results from the net effect of many weak force impulses acting on the slider with a periodicity that is much shorter than the relaxation time constant of the assembly.

Table 3 Model excitation parameters employed to simulate the fluctuating component of the experimental displacement, FFT spectrum, and autocorrelation in Figs. 8–10 in the bridged state

Rotation rate rpm	Pressure kPa	f_0 mN	f_m mN	T_n ms	r_n %
7,200	20	14.2	3.55	0.289	0.05
7,200	60	20.2	3.55	0.50	1.0
1,300	90	33.6	4.80	5.0	50.0

The simulation was able to closely reproduce the nature of the fluctuating displacement, FFT amplitude spectrum, and autocorrelation. The FFT amplitude spectra are compared in Fig. 10. The model spectrum fits the primary resonance peak remarkably well down to more than an order of magnitude from the peak. It is interesting to note that the driven single DOF model with a base-impulse period of 0.289 ms closely matched the frequency and amplitude of the secondary FFT peak at 3,460 Hz in the 7,200 rpm and 20 kPa bridged state displacement spectrum, Fig. 10a.

The model simulated displacement, and the random impulse force series used to simulate the displacement in the bridged state are shown in Fig. 14. Bursts of displacement fluctuations seem to arise from force impulse excitations that are in-phase with the ongoing oscillations of the load beam and slider suspension assembly. Apparent spikes in the displacement at the higher pressure and lower rotation rate are random events that correspond to several impulses which occur in rapid succession. The average displacement does not appear to arise from a series of force pulse with frequencies higher than the resonant frequency because there is a significant average displacement in the bridged state at 1,300 rpm and 90 kPa, Fig. 14c, while the force impulses are relatively much less frequent. Hence the model suggests that the steady component of the displacement is due to a steady component of the friction force, while the fluctuating component is equivalent to a series of force impulses with random frequency and amplitude as described above.

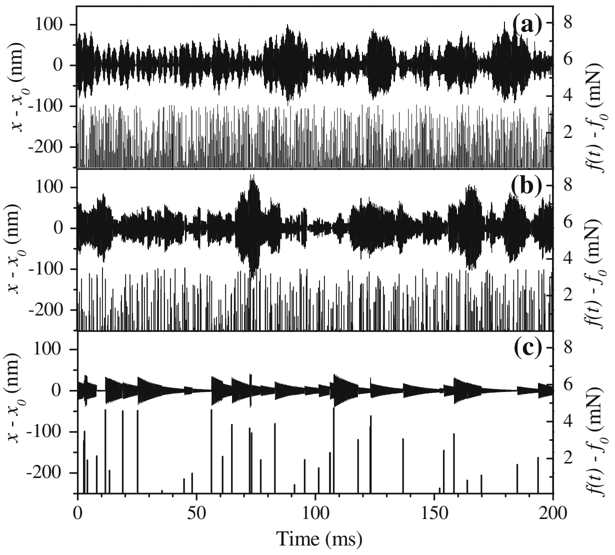

Fig. 14 Fluctuating displacement response calculated from the driven single DOF model and the random impulse force series used to simulate the bridged state at: (**a**) 7,200 rpm, 20 kPa, (**b**) 7,200 rpm, 60 kPa, and (**c**) 1,300 rpm, 90 kPa. These correspond to the measured displacement rotation rate and pressures in Fig. 8

The autocorrelation for the model calculated displacement closely resembles the experimental autocorrelation shown in Fig. 9. After many trials runs of the displacement model, it became apparent that the finer structure of the autocorrelation beyond a lag time of about 25 ms varies randomly with the apparent periodicity of the displacement fluctuation bursts.

4.2 Origin of Friction in the Bridged State

In this section, we solve the force and torque balance on the slider in the bridged state to derive the relationship between the average frictional displacement and the shear stress on the slider in terms of the slider geometry and surface areas. Since the slider geometry is known, and the friction is measured, the two remaining unknown quantities are the bridge adhesion stress, and the bridged area fraction. The interacting portion of the topography, or the bridged area fraction, is calculated from the probability of overlap between the lubricated disk topography and the lubricated (or unlubricated) slider topography. The spacing probability density function (pdf) is derived from the difference between measured slider and disk surface topography pdf.

Adhesion stress in the bridged state is attributed to London dispersion force. A full treatment of the dispersion force in terms of the Lifshitz theory of multilayers is needed to rigorously calculate the mean surface separation in the bridged state. For the scope of this study, we limit our consideration to localized regions of overlapping topography. In this case, the adhesion stress is calculated from the Lifshitz theory for dispersion interaction energy in the limit of zero air gap.

4.2.1 Force and Torque Balance

When the slider is flying normally, the force and torque are balanced such that the slider is in equilibrium. The small frictional displacement during flying (Fig. 8 baseline) is due to air shear. In the bridged state the air bearing on the slider is unchanged; however, there is an extra shear force due to the bridge adhesion force; the suspension load is fully supported by the air bearing, and the bridge torque balance is considered independently of the air-bearing force. The additional shear force and torque are distributed as shown in Fig. 15. As shown later, the transient bridges comprise a very small fraction of the surface area.

Frictional displacement of the load beam arises from the shear stress on parts of the slider which are interacting with the disk through the bridges. As the ambient air pressure is reduced, the pitch, roll, and trailing edge flying height decrease. The trailing edge pad is the closest part of the slider to the disk surface. Thus the friction force in the bridged state arises from shear force on the trailing edge pad. A torque balance on the slider body relates the adhesion force S_{adh} to the friction force S_f. In our case, the pivot point at the gimbaled attachment of the slider body to the suspension is at the top center of the slider body. The torque balance about the pivot point gives the adhesion force $S_{\mathrm{adh}} = mS_f$ where $m = y_s/x_s$ is the torque moment arm ratio, y_s is the slider body thickness, and x_s is the distance between the slider pivot point and the trailing edge pad. These provide the relationship between the experimental friction force and the bridge adhesion stress σ_{adh}:

$$\sigma_{\mathrm{adh}} = \frac{S_{\mathrm{adh}}}{A_b} = \frac{mS_f}{A_b} = \left(\frac{A_{\mathrm{pad}}}{A_b}\right)\left(\frac{m}{A_{\mathrm{pad}}}\right) S_f, \tag{5}$$

where A_b is the bridged area, A_{pad} is the nominal surface area of the pad, and (A_{pad}/A_b) is the bridged area fraction.

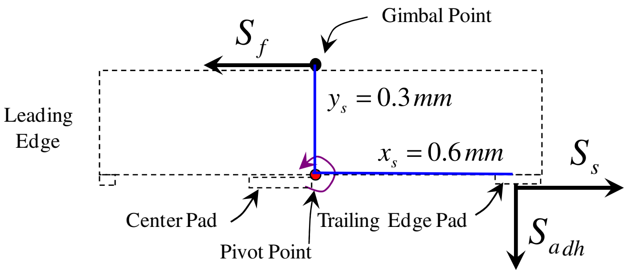

Fig. 15 Free body diagram of the slider, to scale, showing the location of the "bridge" force components adhesion force S_{adh} and the shear force S_s along with the friction force S_f on the suspension. The slider thickness y_s and half length x_s are the moment arms in the torque balance. The normal load of the suspension is not shown because it is offset by the air-bearing lift force

4.2.2 Spacing Probability Density Function

Real slider and disk surfaces have finite surface roughnesses which are each characterized by a surface height probability density function (pdf). The distance between the surfaces is characterized by a spacing pdf, referred to here as the spacing pdf. In this section, we describe the calculation of the spacing pdf from scanning probe microscope image profiles for each of the surfaces. The bridged area fraction is then derived from the spacing pdf.

Scanning probe microscope (SPM) images of the disk and slider are shown in Figs. 16a and b, respectively. The surface height density versus distance normal to the surface from the images is shown in Fig. 16c. A pdf $f(s)$ is equated to the normalized surface height, where $f(s)ds$ is the probability that the surface height is between s and $s + ds$ and s is distance normal to a plane of the surface (slider or disk). The probability density for the slider was flipped with respect to the surface level measured by the SPM because the slider is facing the disk.

Profile sections from the scanning probe microscope images are shown to illustrate the regions of interaction between the surface of the disk lubricant and the slider carbon overcoat in Fig. 17a. Overlapping regions of surface topography, which form the transient bridges, are encircled by dashed ellipses. The molecular diameter of the lubricant chain is indicated by the bar within the disk lube. Note that the overlapping of the upper and lower surfaces is greatly exaggerated for illustration. Air fills the gap between the surfaces outside the regions of overlap. In the bridged state, more than 99% of the gap is gas-filled.

Since the slider may also accumulate a thin film lubricant [33, 34], the slider + lubricant surface level pdf is illustrated in Fig. 16c and 17b. The lubricant thickness is assumed to be uniform. In the example shown, 0.6 nm of lubricant on the slider shifts the mean level of each surface closer by 0.6 nm. In the real system, the mean spacing gap increases with lubricant on the slider due to an increase in the slider flying height [35]. A profile section from the scanning probe microscope image is shown to illustrate the

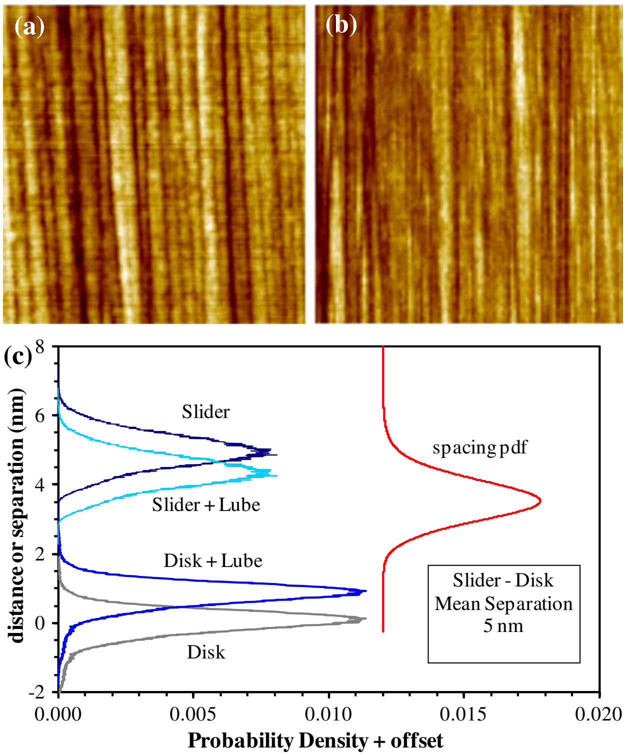

Fig. 16 Scanning probe microscopy image of the disk surface (**a**) and slider trailing pad surface (**b**), both at 1 × 1 micron. Probability density functions for the disk and slider surface height shifted to face one another with mean separation 5 nm, mean disk surface height set to zero, 0.8 nm of lubricant added to the disk surface height, 0.6 nm of lubricant added to the slider surface height, slider-lube separation calculated from slider and lube probability density functions was offset by 0.012 along the horizontal axis for illustration (**c**)

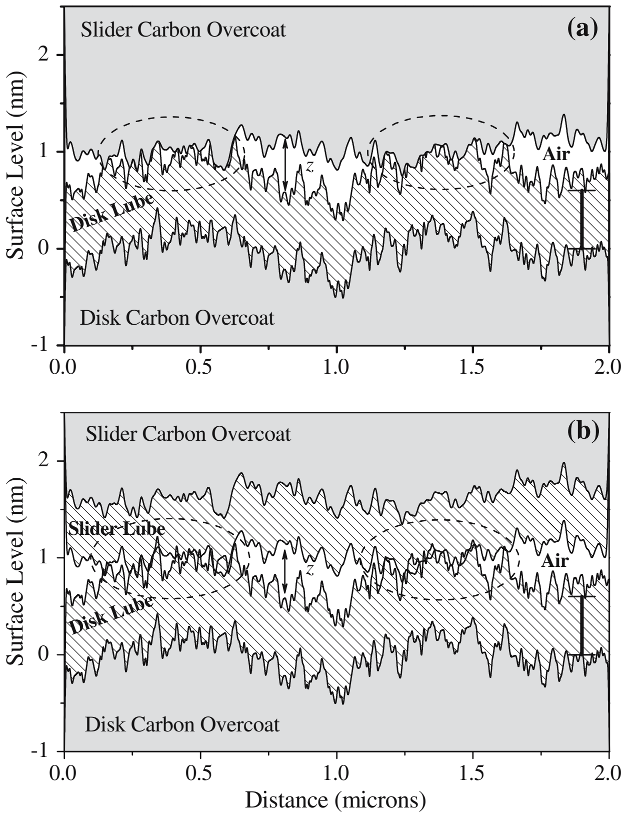

Fig. 17 Profile section of the slider-disk interface from the scanning probe microscope images schematically illustrating the bridged state (**a**) with 0.8 nm of lubricant on the disk, and (**b**) 0.8 nm of lubricant on the disk and 0.6 nm of lubricant on the slider. The bar on the right in the disk lubricant shows the lubricant molecular chain diameter. The slider and disk have been placed artificially close together to exaggerate the regions of overlap which are encircled by the dashed lines

regions of interaction between the surfaces of the disk lubricant and the lubricant on the slider in Fig. 17b. Calculations below are performed for an arbitrary combined lubricant thickness l.

As mentioned above, the slider and disk surface height are random variables. Hence the slider-disk spacing gap is also a random variable. Let x represent the height of a point on the slider surface and y represent the height of a point on the disk surface relative to a reference plane. For convenience, the reference level is taken to be the mean plane of the unlubricated disk surface.

The spacing gap at one point between the two surfaces is $z = x–y$. For example, notice that z is shown within the air gap near the middle of Fig. 17a and b. This illustrates a particular value of the distance that is referred to by z. The pdf for the difference between two random variables is given by [36]

$$f_z(z) = \int_{-\infty}^{\infty} f_x(z - y) f_y(-y)\, dy \qquad (6)$$

In practice, the spacing pdf is numerically determined from the SPM data for the slider $f_x(x)$ and the disk $f_y(y)$ according to

$$T\{f_z(z)\} = T\{f_x(x)\} \times T^{*}\{f_y(y)\}, \qquad (7)$$

where $T\{\}$ indicates Fourier transform and $T^{*}\{\}$ is the complex conjugate of the Fourier Transform. Fast Fourier Transforms, complex operations, and inverse Fast Fourier Transforms were performed on the normalize surface level density data (500 points, 0.041 nm interval) to obtain the measured spacing pdf $f_z(z)$. An example of the spacing pdf is shown in Fig. 16c, where the mean solid surface separation is set to 5 nm. Changes in the flying height or the lubricant thickness only shift $f_z(z)$ along the z-axis. The average, or “expected value” of the separation changes according to $E\{z\} = E\{x\} - E\{y\}$ where $E\{\}$ indicates the expected value and $E\{s\} = \int_{-\infty}^{\infty} s f_s(s) ds$. Bringing the slider closer to the disk shifts $f_z(z)$ to the left along the z-axis. The shifting of the density function is illustrated in Fig. 18a for lubricated slider and disk. The probability of overlap between the lubricated slider and disk probability density is the area under the $f_z(z)$ curve in the region where $z < 0$.

When the combined lubricant thickness on the disk and slider is l and the mean solid surface spacing between the slider and disk is h, the spacing variable becomes $z^* = z - h + l$. The probability of points on the two surfaces overlapping one another is

$$P\{z* < 0\} = \int_{-\infty}^{0} f_z(z*)dz* = F_z(l - h), \qquad (8)$$

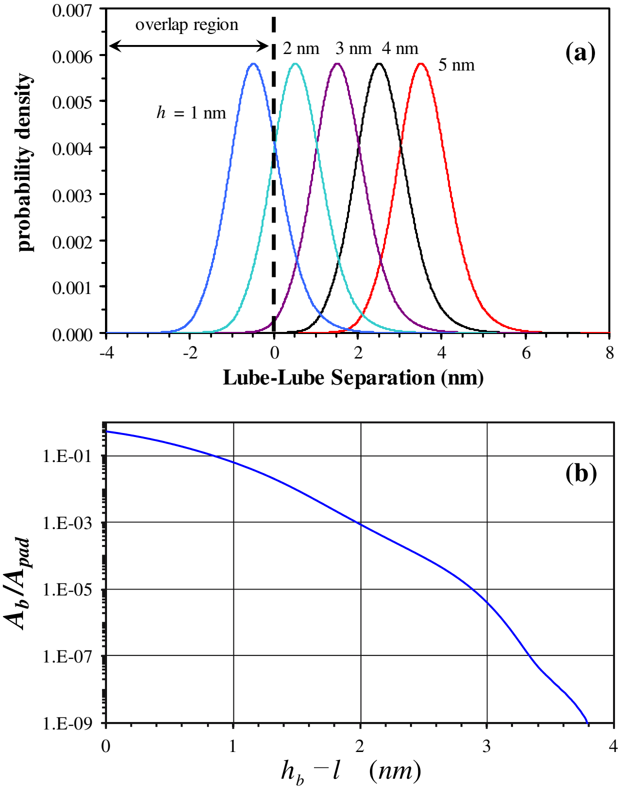

Fig. 18 (**a**) Probability density for the separation between the 0.8 nm thick lubricant films on the disk and a 0.6 nm thick lubricant film on the slider. The lubricant films are in contact for the region of the density function when the separation is less than zero. (**b**) bridged area fraction versus the mean bridge spacing gap—lubricant thickness

where $F_z(z)$ is the cumulative distribution function, and the bridged fraction of the trailing pad area is approximately given by $A_b/A_{\text{pad}} = P\{z^* < 0\}$. This ratio is shown plotted as function of $h_b - l$ in Fig. 18b, where h_b is the mean solid surface separation in the bridged state, or bridge spacing gap. The overlap probability increases with decreasing mean (unlubricated) slider-disk separation h_b, and drops of by orders of magnitude with increasing slider-disk separation. With reference to Eq. (5), the slope of the curve in Fig. 18b plot provides the bridge stiffness $k_b = \partial S_a/\partial h_b$.

4.2.3 Adhesion Stress

In a transient bridge between two asperities, as depicted by the encircled regions in Fig. 17, the surfaces are still being laterally displaced at nominally 10 m/s. The experimental time scale is approximately the ratio of a characteristic molecular length scale to the sliding velocity [37], which is *c.a.* 20 ps for the subambient pressure friction test. This is much shorter than the time scale for cooperative motion (> 400 ns) [30], thus stick slip through interdiffusion such as that observed at low-velocity sliding of grafted chain monolayers [38] is absent from the bridged state in our tests. The premise of the molecular adhesion model is as follows. Within the short-time scale of a transient "bridge" between two asperities, the lubricant chains respond as solid-like with respect to interdiffusion, and the shear planes translate laterally by slipping relative to one another in presence of dispersive adhesion stress. The dominant contributions to the dispersion are in the ultraviolet and infrared. Dispersion force operates on a time scale (10^{16}–10^{14} rad/sec), which is much shorter than the lifetime of the transient bridges. Only dispersion force contributions to the tensile strength are included in the following, because the high velocity between the slider and disk asperities does not allow time for dipole orientation [26], and there are relatively few polar end groups per unit area of disk surface [39].

The interaction free energy per unit area between two material surfaces separated by a planar gap is [40, 41]:

$$E = \frac{kT}{2\pi}\sum_{n=0}^{\infty}{}' \int_0^{\infty} \rho\, d\rho\, \ln G(\xi_n) \tag{9}$$

where k is the Boltzmann constant, T is absolute temperature, ρ is the surface mode wave vector, $\xi_n = n(2\pi kT/\hbar)$, and $\hbar$ is the reduced Planck constant. When the spacing gap is thickness L, the force per unit area across the gap is [42]:

$$\Pi = -\frac{\partial E}{\partial L} = -\frac{kT}{2\pi}\sum_{n=0}^{\infty}{}' \int_0^{\infty} \rho\, d\rho\, \frac{1}{G(\xi_n)}\frac{\partial G(\xi_n)}{\partial L}. \tag{10}$$

The prime on the summation indicates that the $n = 0$ term is given half weight. In the case of an air gap between the lubricated disk and the unlubricated slider $G(\xi_n) = 1 - \Delta_{la}\Delta_{ca}e^{-2\rho L}$. In the case of an air gap between the lubricated disk and a lubricated slider $G(\xi_n) = 1 - \Delta_{la}^2 e^{-2\rho L}$. Subscript l denotes lubricant, a is for air, and c is for the carbon overcoat. The Δ_{la} and Δ_{ca} are functions of the dispersion spectrum for each material pair and they will be defined later. (Here we consider only the upper layers in the dispersion force calculation.)

Following Hough and White [43], we invoke a cutoff wave number ρ_c above which the dispersion interaction decreases rapidly to zero. Physically this represents the lower wavelength limit for absorption due to the finite molecular dimensions of the material. For interaction energy between two dissimilar materials such as lubricant and the carbon overcoat, we select the shorter of the two cutoff wavelengths because of this limitation.

The bridge adhesion stress is then the limiting case of Eq. (10) air gap $L \to 0$, or $\sigma_{\text{adh}} = -\Pi(L \to 0)$. For a bridge between the lubricated disk and an unlubricated slider:

$$\sigma_{adh}(\text{unlubed slider}) = \frac{kT}{3\pi}\rho_c^3 \sum_{n=0}^{\infty}{}' \frac{\Delta_{la}\Delta_{ca}}{1 - \Delta_{la}\Delta_{ca}} \tag{11}$$

And for a bridge between the lubricated disk and a lubricated slider:

$$\sigma_{adh}(\text{lubed slider}) = \frac{kT}{3\pi}\rho_c^3 \sum_{n=0}^{\infty}{}' \frac{\Delta_{la}^2}{1 - \Delta_{la}^2}. \tag{12}$$

Since ρ_c is unknown, it is calculated from the dispersive surface energy [43, Eq. (7.24)]. The lubricant dispersive surface energy:

$$\gamma_l^d = -\frac{kT}{8\pi}\rho_c^2 \sum_{n=0}^{\infty}{}' \ln\left(1 - \Delta_{la}^2\right), \tag{13}$$

and the dispersive surface energy of the carbon overcoat:

$$\gamma_c^d = -\frac{kT}{8\pi}\rho_c^2 \sum_{n=0}^{\infty}{}' \ln\left(1 - \Delta_{ca}^2\right). \tag{14}$$

Before calculating the surface energy and adhesion stress, it is necessary to define the quantities Δ_{la} and Δ_{ca}. The definition arises from a solution of Maxwell's equations and summing the allowed normal mode frequencies [41]:

$$\Delta_{la} = \frac{\varepsilon_l(i\xi_n) - 1}{\varepsilon_l(i\xi_n) + 1}, \tag{15}$$

and

$$\Delta_{ca} = \frac{\varepsilon_c(i\xi_n) - 1}{\varepsilon_c(i\xi_n) + 1}, \tag{16}$$

where $i = \sqrt{-1}$, $\varepsilon_l(i\xi_n)$ is the dispersion spectrum of the lubricant, and $\varepsilon_c(i\xi_n)$ is the dispersion spectrum of the carbon overcoat. The dispersion spectrum of air is taken to be 1.

The dispersion spectrum of the lubricant is provided in White et al. [42, Fig. 2], and the dispersion spectrum of the carbon overcoat is provided as a:CH in Dagastine et al. [44, Fig. 2]. The literature values for the dispersion spectra were fit using a two-frequency Ninham–Parsegian construction [41, 43]:

$$\varepsilon(n) = 1 + \frac{P_1}{1 + P_2\, n^2} + \frac{P_3}{1 + P_4\, n^2}, \tag{17}$$

where P_i are fitting parameters (Table 4). The Ninham–Parsegian coefficients can be derived from the UV and IR absorption spectra, the refractive index as a function of wavelength through a Cauchy plot [43], or from the interband transition strength measured with electron energy-loss spectroscopy [40].

As mentioned above, the cutoff wavelength is calculated from the dispersive surface energy for the carbon overcoat and lubricant. The dispersive surface energies γ^d and cutoff

Table 4 Coefficients for the dispersion spectra of lubricant and carbon overcoat from the two-frequency Ninham–Parsegian construction, Eq. (17)

Coefficient	Lubricant	Carbon overcoat
P_1	1.805	1.06366
P_2	0.3696	5.12E-03
P_3	0.6799	1.54326
P_4	3.60E-04	1.70E-04

Table 5 Experimental dispersive surface energies [45] and calculated cutoff wavelengths for lubricant and carbon overcoat

Quantity	Lubricant	Carbon overcoat	Units
γ^{d}	13	43	mN/m
$1/\rho_{c}$	0.221	0.278	nm

wavelengths $1/\rho_c$ for the carbon and lubricant from Eqs. (13 and 14) are listed in Table 5. These cutoff wavelengths are close to those reported for alkanes [43].

The bridge adhesion stress is then calculated from Eqs. (11 and 12), and is listed in the first row of Table 6. The adhesion stress for the unlubricated slider is higher than that for the lubricated slider because the dispersion interaction energy between the lubricant and the carbon overcoat is higher than that between two layers of lubricant.

Now that the bridge adhesion stress is known, Eq. (4) is solved for the bridged area fraction $A_b/A_{\text{pad}} = (m/A_{\text{pad}})(S_f/\sigma_{\text{adh}})$. At the TDP in the bridged state $S_f = f_0 = 33.6\ mN$ from Table 3. The torque moment arm ratio for the slider $m = 0.5$, and the trailing edge pad area $A_{\text{pad}} = 0.014\ mm^2$. These equations provide the bridged area fraction listed in the third row of Table 6. The bridged area fraction increases because the bridge adhesion stress is decreased by the presence of lubricant on the slider.

So far we have found the surface area fraction that is involved in the bridges which give rise to the high friction force at the TDP. The surface topography distributions were measured with AFM and transformed into the spacing pdf. The distance between the mean surface planes of the slider and the disk, the lubricant film thickness on the disk (and slider), and the details of the surface topography were used to determine the spacing between the mean surface planes of the disk and slider. The probability that the spacing between the two surfaces is less that zero was equated to the bridged area fraction A_b/A_{pad}, and this is shown plotted as a function of the difference between the mean bridge spacing gap and the total lubricant thickness $h_b - l$ in Fig. 18b. Placing the experimental values of A_b/A_{pad} from Table 6 along the vertical axis in Fig. 18b, the values of $h_b - l$ are determined by the intersection with the curve along the horizontal axis. The bridged area fraction decreases with increasing (bridge spacing gap—total lubricant thickness). Alternatively, for a given lubricant thickness, the bridge spacing gap increases with decreasing bridged area fraction. The lubricant thicknesses are then employed to determine the mean bridge spacing gap h_b, which is listed in row 4 of Table 6 with and without lubricant on the slider. The bridge spacing gap is larger for the unlubricated slider because the measured average friction force at the TDP (Table 3) is independent of the assumption about whether or not lubricant is present on the slider. The reduced adhesion stress with lubricant on the slider increases the bridged area to obtain the same force by decreasing the mean spacing gap. The values for the adhesion stress and bridge spacing gap at the TDP are nearly the same as those calculated by a simple approximation using the dispersive surface energies and distance of closest approach [45]. (Note that there is a typographical error in Table 2 of Ref. [45]: the values of bridge spacing gap for with and without lubricant on the slider are transposed.)

4.2.4 *Lubricant Transfer Between Disk and Slider*

Beyond determination of the bridge spacing gap from the fractional contact area, further insight is also provided by the shifted spacing curve in Fig. 18b. A small but finite amount of overlap between lubricant on asperity tips is expected even out to $h_b - l \geq 3$ nm. For 1 nm of lubricant on the disk, this is a mean solid surface separation of 4 nm. Critical flying heights for the onset lubricant transfer have been reported [27]. The value of the critical flying height is partly determined by the slider design. The critical flying height for the onset of lubricant transfer would also be expected to depend on the details of the slider and disk surface topography. Evaporation has been proposed to account for lubricant transfer from disk to slider [46, 47]. It is also likely that lubricant is transferred during fractional area contacts such as those expected from Fig. 18b, and schematically illustrated in Fig. 17.

Table 6 Bridged state slider-disk quantities at the TDP calculated with 0.8 nm of lubricant on the disk and none or 0.6 nm of lubricant on the slider. The torque moment arm ratio $m = 0.5$

Quantity	Symbol	Unlubricated slider	Lubricated slider	Units
Bridge adhesion stress	σ_{adh}	356	165	MPa
Bridge shear stress	σ_{f}	712	330	Mpa
Bridged fraction	$\text{A}_{\text{b}}/\text{A}_{\text{pad}}$	0.33	0.72	%
Mean solid surface separation	h_b	3.0	2.5	nm

Table 7 Hamaker constants calculated from Lifshitz theory for the different combinations of interface materials in the limit of zero air gap

Material combination	Hamaker constant (J)
Lube-air-lube	2.30E-20
Lube-air-carbon	4.85E-20
Carbon-air-carbon	1.11E-19

A measure of the interaction energy is provided by the Hamaker constant. The Hamaker constants were calculated from the Lifshitz theory [43] as above. In the limit of zero air gap, Hamaker constants for the various combinations of lubricant and carbon overcoat are listed in Table 7. These show that the dispersion interaction energy between the lubricant and the overcoat is about 2× larger than that between the lubricant chains themselves. When a lubricant chain on the disk bridges to the unlubricated slider carbon overcoat, it is energetically favorable for that chain to transfer to the slider overcoat. Once lubricant chains transfer to the slider overcoat, they are sheared back to the trailing end of the slider [46] in the airflow. Lubricant chains that are in a monolayer on the disk surface have equal dispersion interaction energy between the slider and disk carbon overcoats only if the overcoats have identical dispersion spectra. Lubricant chains that are physisorbed or chemisorbed by polar or reactive end groups possess an additional contribution to the interaction energy with the overcoat that decreases the probability of chain transfer.

4.2.5 *Frictional Energy Dissipation*

The preceding sections focused on the friction, adhesion stress, and flying height in the bridged state at the touchdown pressure. It is also of interest to consider the remaining portion of the subambient pressure frictional hysteresis loop at this point in the discussion. The friction force increases along the increasing pressure branch of the hysteresis loop in the bridged state, as shown in Fig. 6. This trend is always observed with a wide range of commercial grade sliders, disks, and lubricants. An increase in the friction force along this branch of the loop reflects an increase in the frictional energy dissipation with increasing pressure. This is contrary to what one might expect. Increasing the air pressure above the TDP increases the air-bearing lift force. The increase in lift force is expected to increase the spacing gap (flying height), traversing from left to right along the curve in Fig. 18b. The bridge area fraction is then expected to decrease. If the adhesion stress remains constant, the friction force should decrease, which is the opposite of what is always observed. In the absence of bridge interactions, the attractive dispersion force per unit area decreases monotonically with increasing air gap [42].

Within the context of our analysis which attributes the friction force in the bridged state to dispersion force within transient bridges during intermittent lubricated asperity interactions, an increase in the friction force with ambient pressure implies an increase in the adhesion stress. A mechanism which could give rise to this observation is described in the following. For bulk Ztetraol 2000, the viscoelastic shear loss tangent at 10^9 Hz and 20 °C is 1.22×10^{-5} [26], so that the strain energy stored in the asperity contact is almost fully recovered. Only 0.00122% is immediately lost to viscous dissipation. Molecular processes that are rapid enough to store elastic energy in a 9 ns or less contact time scale are bond vibration (10^{-4} ns) and torsional rotation about the C–O bond [48]. Elastic energy is stored as perturbations to the equilibrium molecular bond vibration amplitudes and torsion angles. The stored energy may be dissipated through radiation or phonon transport [49, 50]. More recently, surface vibration dissipation modes have been shown to contribute significantly to the friction between diamond and silicon [51].

How could these phenomena account for an increase in the dispersive adhesion stress? As shown above in the Lifshitz theory for the dispersive adhesion stress, Eqs. (11 and 12), the adhesion stress is proportional to a sum over the dispersion spectrum of the lubricant $\varepsilon_l(i\xi_n)$. The dispersion spectrum is determined by the values of the coefficients in the two-parameter Ninham–Parsegian construction, Eq. (17). In terms of relaxation frequencies, the coefficients P_2 and P_4 indicate that the primary contribution to the dispersion spectrum for the lubricant is in the UV. In this case the oscillator strengths P_1 and P_3 are approximately proportional to the square of the refractive index in the visible region of frequency [43]. Since the refractive index for the lubricant is a function of the shear stress through orientation of chain subsituents [52], shear stress could increase the adhesion stress. Typically the friction increases by 1.5× as the pressure is increased above the TDP, Fig. 6. With lubricant on the slider, a 1.5× increase in the adhesion stress could be accounted for by a 1.3× in the oscillator strengths. This corresponds approximately to an increase in the lubricant refractive index from 1.3 to 1.382 due to stress orientation.

4.2.6 *Fluctuating Friction Force and Disk Indentations*

The average friction force in the bridged state is accounted for by the dispersion force interaction between the lubricated disk and slider surface topographies. However, fluctuations in the load beam displacement also indicate that there are random impulses in the adhesion force with well-defined characteristics, Eq. (4) and Table 3. On the microscopic scale, the most likely origin for the force impulse is sudden changes in the disk surface topography as the track passes underneath the slider. In the bridged state in the first row of Table 3, the maximum impulse force amplitude is 3.55 mN on an average force of 14.2 mN. This corresponds to impulse changes of 25% in the bridged area fraction A_b/A_{pad} in Eq. (5).

The presence of disk indentations in the test track provides evidence for an occasional force impulse as high as 10 N, Table 2. The maximum adhesion force calculated from the adhesion stress is 5 N for an unlubricated slider and 2 N for a lubricated slider. This apparent anomaly can be accounted for through the impact mechanism of Tao et al. [2], which predicts the growth of plastic deformation in the region peripheral to the contact where the von Mises equivalent stress exceeds the yield strength. The contact loads in their finite element model were 300 and 500 grams, which is about half of our equivalent load in Table 2.

5 Summary and Conclusions

As the ambient pressure is decreased with the magnetic recording slider initially flying over the lubricated disk surface, there is a sudden transition to high friction and vibration (bridged state) at some low touchdown pressure. As the pressure is increased, the high friction state persists well above the touchdown pressure before returning to the flying state. The friction pressure curve forms a subambient pressure frictional hysteresis loop. In hysteresis loop tests performed over a range of disk rotation rate, the transition to the bridged state occurred at the same flying height, independent of linear velocity. The head suspension strain gage assembly was modeled as a single degree of freedom linear spring mass dashpot equivalent mechanical system to determine the equivalent excitation function from the strain gage. While in the bridged state, there is a steady force and a series of force impulses with random period and amplitude.

During several hysteresis loop tests, optical surface analysis detected less than 0.03 nm of lubricant removal from the test track, and no overcoat damage or wear debris. However, evidence for occasional impact of the leading edge pads by a sudden pitch down of the slider was observed. The impact events formed shallow indentations in the disk. Optical interference profilometry detected a slight rounding on the front edges of the circular leading edge pads of the slider.

On the time scale of an asperity contact in the bridged state, the lubricant is viscoelastic solid-like. The Lifshitz theory for dispersion interaction was employed to derive the adhesion stress. The slider and disk surface spacing pdf was derived from the measured surface topographies to obtain the bridged area fraction. These were combined with the average friction force to calculate the mean spacing at the touchdown pressure.

An increase in the friction force with pressure along the increasing pressure branch of the hysteresis loop is consistent with a stress-induced increase in the oscillator strength of the lubricant molecular orbitals.

Force impulses are consistent with point–to-point variations in the surface topography around the disk circumference. Occasional indentations suggest impact force on the order of Newtons, and these can be accounted for by occasional regions of surface topography with a high-bridged area fraction.

Lubricant transfer to low-flying sliders can be accounted for by a higher dispersive interaction energy between the carbon overcoat than between the lubricant chains themselves, and slight overlap of the slider and disk surface topographies. This is quantified in terms of the spacing pdf.

Friction force between the low-flying slider and a molecularly thin film of perfluoropolyether lubricant can be fully accounted for by dispersion force without invoking the presence of a liquid meniscus.

Acknowledgments We thank B. Marchon, P. Baumgart, M. Mate, V. Nayak, R. Payne, B. Knigge, F. Hendriks, and Q. Dai for technical discussions. The authors are also grateful to J. He, R. White, J. Hopkins, and R-H. Wang for their assistance with the investigations of surface indentations.

References

1. Yuan, Z-M., Liu, B., Wang, J.: Flash temperature induced magnetic degradation in high density magnetic recording. J. Appl. Phys. **87**, 6158–6160 (2000)
2. Tao, Q., Lee, H.P., Lim, S.P.: Contact analysis of impact in magnetic head disk interfaces. Tribol. Int. **36**, 49–56 (2003)
3. Thornton, B.H., Bogy, D.B.: Head-disk interface dynamic instability due to intermolecular forces. IEEE Trans. Magn. **39**, 2420–2422 (2003)
4. Ambekar, R., Gupta, V., Bogy, D.B.: Experimental and numerical investigation of dynamic instability in the head disk interface at proximity. J. Tribol. **127**, 530–536 (2005)
5. Kato, T., Watanabe, S., Matsuoka, H.: Dynamic characteristics of an in-contact head slider considering meniscus force: part 1—formulation and application to the disk with sinusoidal undulation. J. Tribol. **122**, 633–638 (2000)
6. Kato, T., Watanabe, S., Matsuoka, H.: Dynamic characteristics of an in-contact head slider considering meniscus force: part 2—application to the disk with random undulation and design conditions. J. Tribol. **123**, 168–174 (2001)
7. Tanaka, H., Yonemura, S., Tokisue, H.: Slider dynamics during continuous contact with textured and smooth disks in ultra low flying height. IEEE Trans. Magn. **37**, 906–911 (2001)
8. Mate, C.M., Arnett, P.C., Baumgart, P., Dai, Q., Guruz, U.M., Knigge, B.E., Payne, R.N., Ruiz, O.J., Wang, G.J., Yen, B.K.: Dynamics of contacting head-disk interfaces. IEEE Trans. Magn. **40**, 3156–3158 (2004)
9. Xu, J.G., Kohira, H., Tanaka, H., Saegusa, S.: Partial-contact head-disk interface approach for high-density recording. IEEE Trans. Magn. **41**, 3031–3033 (2005)

10. Ono, K., Ohara, S.: Experimental identification of elastic, damping and adhesion forces in collision of spherical sliders with stationary magnetic disks. J. Tribol. **127**, 365–375 (2005)
11. Ono, K., Yamane, M., Yamaura, H.: Experimental and analytical study of bouncing vibrations of a flying head slider in a near-contact regime. J. Tribol. **127**, 376–386 (2005)
12. Mayeed, M.S., Kato, T., Jhon, M.S., Mitsuya, Y.: Surface perturbations on the perfluoropolyether molecules in the melt and the gas-like conditions. IEEE Trans. Magn. **40**, 3180–3182 (2004)
13. Matsuoka, H., Ohkubo, S., Fukui, S.: Corrected expression of the van der Waals pressure for multilayered system with application to analyses of static characteristics of flying head sliders with an ultrasmall spacing: Microsyst Techn. Micro Nanosyst—Inf. Stor. Proc. Syst. **11**, 824–829 (2005)
14. Tanaka, K., Kato, T., Matsumoto, Y.: Molecular dynamics simulation of vibrational friction force due to molecular deformation in confined lubricant film. J. Tribol. **125**, 587–591 (2003)
15. Kamei, D., Zhou, H., Suzuki, K., Konno, K., Takami, S., Kubo, M., Miyamoto, A.: Computational chemistry study on the dynamics of lubricant molecules under shear conditions. Tribol. Int. **36**, 297–303 (2003)
16. Khurshudov, A., Baumgart, P., Waltman, R.J.: In-situ quantitative analysis of nano-scale lubricant migration at the slider-disk interface. Wear **229**, 690–699 (1999)
17. Khurshudov, A., Waltman, R.J.: The contribution of thin PFPE lubricants to slider-disk spacing. Tribol. Lett. **11**, 143–149 (2001)
18. Waltman, R.J., Khurshudov, A.G.: The contribution of thin PFPE lubricants to slider-disk spacing. 2. effect of film thickness and lubricant end groups. Tribol. Lett. **13**, 197–202 (2002)
19. Novotny, V.J.: Mechanical integration of high recording density drives. IEEE Trans. Magn. **32**, 1826–1831 (1996)
20. Karis, T.E., Tawakkul, M.A.: Water adsorption and friction on thin film magnetic recording disks. Tribol. Trans. **46**, 469–478 (2003)
21. Karis, T.E., Nayak, U.V.: Liquid nanodroplets on thin film magnetic recording disks. Tribol. Trans. **47**, 103–110 (2004)
22. Karis, T.E., Kim, W.T., Jhon, M.S.: Spreading and dewetting in nanoscale lubrication. Tribol. Lett. **18**, 27–41 (2005)
23. Tagawa, N., Mori, A.: Effects of functional end-groups on nanotribology characteristics of ultra-thin liquid lubricant films in hard disk drives. IEEE Trans. Magn. **41**, 825–830 (2005)
24. Bai, M., Kato, K.: Analysis of contact deformation and stiction between textured disk and textured slider. J. Tribol. **123**, 350–357 (2001)
25. Suh, A.Y., Polycarpou A.: Adhesive contact modeling for sub-5-nm ultralow flying magnetic storage head-disk interfaces including roughness effects. J. Appl. Phys. **97**, 104328-1–104328-11 (2005)
26. Karis, T.E.: Lubricants for the disk drive industry. In: Rudnick, L. (ed.), Synthetic, Mineral Oil, and Bio-Based Lubricants Chemistry and Technology, CRC Press, Taylor & Francis Group, LLC, Boca Raton, FL, pp. 623–654 (2006)
27. Ambekar, R.P., Bogy D.B., Dai Q., Marchon B.: Critical clearance and lubricant instability at the head-disk interface of a disk drive. Appl. Phys. Lett. **92**, 033104-1–033104-3 (2008)
28. Crone, R.M., Peck, P.R., Jhon, M.S., Karis, T.E.: Scaling criteria for slider miniaturization using the generalized reynolds equation. J. Tribol. **115**, 566–572 (1993)
29. Karis, T.E., Guo, X.-C., Marinero, E., Marchon, B.: Surface chemistry of NiP plated substrates. IEEE Trans. Magn. **41**, 3247–3249 (2005)
30. Karis, T.E.: Tribochemistry in contact recording. Tribol. Lett. **10**, 149–162 (2001)
31. Karis, T.E.: Water adsorption on thin film magnetic recording media. J. Coll. Int. Sci. **225**, 196–203 (2000)
32. Man, Y.J., Yu S.K., Liu B.: Characterization and formation mechanism understanding of asperities to be burnished. J. Magn. Magn. Mater. **303**, e101–e105 (2006)
33. Fred Li, Z., Chen, C-Y., Liu, J.J.: Study of head-disk interference at low-flying height. IEEE Trans. Magn. **39**, 2462–2464 (2003)
34. Marchon, B., Karis, T., Dai, Q., Pit, R.: A model for lubricant flow from disk to slider. IEEE Trans. Magn. **39**, 2447–2449 (2003)
35. Ma, X., Chen, J., Richter, H.J., Tang, H., Gui, J.: Contribution of lubricant thickness to head—media spacing. IEEE Trans. Magn. **37**, 1824–1826 (2001)
36. Papoulis, A.: Probability, Random Variables, and Stochastic Processes, McGraw-Hill Book Company, New York, NY (1965)
37. Yoshizawa, H., Chen, Y-L., Israelachvili, J.: Fundamental mechanisms of interfacial friction. 1. relation between adhesion and friction. J. Phys. Chem. **97**, 4128–4140 (1993)
38. Persson, B.N.J.: Theory of friction: friction dynamic for boundary lubricated surfaces. Phys. Rev. B **55**, 8004–8012 (1997)
39. Yatsue, T., Ishihara, H., Matsumoto, H., Tani, H.: Design of carbon surface functional groups on the viewpoint of lubricant layer structure. Trib. Trans. **43**, 802–808 (2000)
40. French, R.H.: Origins and applications of london dispersion forces and hamaker constants in ceramics. J. Am. Ceram. Soc. **83**, 2117–2146 (2000)
41. Ninham, B.W., Parsegian, V.A.: Van der walls forces across triple-layer films. J. Chem. Phys. **52**, 4578–4587 (1970)
42. White, L.R., Dagastine, R.R., Jones, P.M., Hsia Y-T.: Van der waals force calculation between laminated media, pertinent to the magnetic storage head-disk interface. J. Appl. Phys. **97**, 104503 (2005)
43. Hough, D.B., White, L.R.: The calculation of hamaker constants from lifshitz theory with applications to wetting phenomena. Adv. Coll. Int. Sci. **14**, 3–41 (1980)
44. Dagastine, R.R., White, L.R., Jones, P.M., Hsia Y-T.: Effect of media overcoat on van der waals interaction at the head-disk interface. J. Appl. Phys. **97**, 126106 (2005)
45. Karis, T.E., Guo X-C.: Molecular adhesion model for the bridged state of a magnetic recording slider. IEEE Trans. Magn. **43**, 2232–2234 (2007)
46. Marchon, B., Karis, T., Dai, Q., Pit, R.: A model for lubricant flow from disk to slider. IEEE Trans. Magn. **39**, 2447–2449 (2003)
47. Ma, Y.S., Liu, G.: Lubricant transfer from disk to slider in hard disk drives. Appl. Phys. Lett. **90**, 143516 (2007)
48. Waltman, R.J., Tyndall, G.W., Pacansky, J., Berry, R.J.: Impact of polymer structure and confinement on the kinetics of zdol 4000 bonding to amorphous-hydrogenated carbon. Tribol. Lett. **7**, 91–102 (1999)
49. Aranson, I.S., Tsimring, L.S., Vinokur, V.M.: Stick-slip friction and nucleation dynamics of ultrathin liquid films. Phys. Rev. B **65**, 125402 (2002)
50. Narumanchi, S.V.J., Murthy, J.Y., Amon, C.H.: Boltzmann transport equation-based thermal modeling approaches for hot-spots in microelectronics. Heat Mass Transfer **42**, 478–491 (2006)
51. Cannara, R.J., Brukman, M.J., Cimatu, K., Sumant, A.V., Baldelli, S., Carpick, R.W.: Nanoscale friction varied by isotopic shifting of surface vibrational frequencies. Science **318**, 780–783 (2007)
52. Mriziq, K.S., Dai, H.J., Dadmun, M.D., Jellison, G.E., Cochran, H.D.: High-shear-rate optical rheometer. Rev. Sci. Instr. **75**, 2171–2176 (2004)